Supporting information

In situ hollow nanoarchitectonics of MIL-88A@$Co(OH)_2$ composites for supercapacitor and oxygen evolution reaction

Shuyao Jiang[1,2#], Shuke Li[1#], Zhejun Liu[3], Yanchao Xu[1], Yubin Zhang[1], Ling Zhang[1], Yanqiu Xu[1,2], Shasha Li[1], Yang Jiao[1,2,3*], Jianrong Chen[1,2*]

1 College of Chemistry and Life Science, Zhejiang Normal University, Jinhua, 321004, China.

2 College of Geography and Environmental Sciences, Zhejiang Normal University, Jinhua, 321004, China.

3 Zhejiang Anke Environmental Protection Technology Co., Ltd, China

∗Corresponding author: Yang Jiao and Jianrong Chen; E-mail: yangjiao@zjnu.edu.cn and cjr@zjnu.cn. Fax: (+86)-0579-82291275.

#These two authors contributed equally.

1. Experimental

1.1. Preparation of MIL-88 A, $Co(OH)_2$ and Fe-FA@$Co(OH)_2$

Fe-FA was prepared according to previous literature[1]. 1.2 mmol fumaric acid was dissolved in 25 mL deionized water, and magnetically agitated for 10 min in 70 °C water bath, after which 1.3 mmol $Fe(NO)_3 \cdot 9H_2O$ was added and stirring was continued for another 10 min. After chemicals are completely dissolved, the above solution was placed to 40 mL Teflon-lined stainless-steel autoclave, and kept at 110 °C with 6h. The as-prepared sample was washed several times with deionized water and ethanol, collected by centrifugation and dried at 60 °C overnight after the reaction had cooled to room temperature.

The Fe-FA@$Co(OH)_2$ was synthesized via conventional hydrothermal method. Under magnetic stirring, the reaction solution was made by mixing 0.3 g Fe-FA, 0.2 mol L^{-1} $Co(NO_3)_2 \cdot 6H_2O$ and 0.06 mol L^{-1} $(CH_2)_6N_4$ in 30 mL deionized water. Then this mixed solution was placed into a 50 mL Teflon-lined stainless-steel autoclave and retained under 100 °C for 5h. Subsequently, Fe-FA@$Co(OH)_2$ was rinsed with deionized water before being dried at 60 °C overnight. The same approach as above was used to prepare $Co(OH)_2$ with the exception that Fe-FA was added to the solution.

1.2. Materials Characterization

All materials are investigated by Scanning Electron Microscope (SEM, Gemini SEM 300) and Energy-Dispersive X-ray (EDX) spectrometer. The

interior structure of materials is further investigated using transmission electron microscopy (TEM, JEM-2100F). The composition and crystallinity of materials were studied by X-ray diffraction (XRD, Bruker, D8 Advance) with Cu Kα radiation. X-ray photoelectron spectroscope (XPS) measurement were performed on a Thermo Scientific ESCALAB 250Xi spectrometer to analyze the elemental composition and valence distribution of the composite materials (carbon calibration is 284.8 eV). The functional group composition of materials was analyzed using Fourier transform infrared spectroscopy (FTIR, Thermo Nicolet, NEXUS 670). Thermogravimetric analysis (TGA) curves were collected on STA449 F5 under N_2 atmosphere with a heating rate of 10 $^oC\ min^{-1}$ from 25 ^oC to 800 ^oC to analyze the thermal stability of materials. The nitrogen adsorption-desorption isotherm at 77k was used to obtain specific surface area and pore size distribution.

1.3. Electrochemical measurements

Electrochemical workstation (CHI 660E) and Neware Batter Tester as test instruments for evaluating electrochemical performance of materials, the detail contents are in supporting information.

1.3.1 Supercapacitor

Materials properties were tested in a three electrodes system on the electrochemical workstation (CHI 660E) and Neware Battery Tester. Materials was used as work electrode, Hg/HgO electrode was used as reference electrode and Pt foil as counter electrode on 3 M KOH solution, respectively. Cyclic voltammetry (CV),

galvanostatic charge-discharge (GCD), electrochemical impedance spectroscopy (EIS) and stability test were the indicators to detect the electrochemical performance of materials.

The working electrodes were prepared by mixing the active material (80%), carbon black (20%) and 5% of polyvinylidene difluoride (20%). The obtained slurry was painted on nickel foam (1 cm × 1 cm) followed by drying at 120℃ for 12h in a vacuum.

The specific capacitance (C) was estimated according to equation (1):

$$C = \frac{I \times \Delta t}{M \times 3600} \quad (1)$$

where C is the specific capacity (mAh g^{-1}), I is the current (A), Δt is discharge time (s), and M is the mass of the active materials (g), respectively.

Assembly of hybrid asymmetric supercapacitor

Fe-FA@$Co(OH)_2$ as positive electrode, active carbon as negative electrode, and 3M KOH aqueous solution as electrolyte to assemble hybrid supercapacitors. The fabrication of negative electrode was used the same method. The electrochemical measurements including CV, GCD and stability test. The GCD was measured between 0 to 1.6 V at different current densities. The specific capacitance (C) was estimated according to equation (2):

$$C = \frac{I \times \Delta t}{M \times \Delta V} \quad (2)$$

where C (F g^{-1}) is the specific capacitance (F g^{-1}), I is the discharge current (A), Δt means the discharge time (S), ΔV is the potential range (V), and M (g) represent

active materials mass, respectively. The power density (P) and energy density (E) were calculated according to equations (4) and (5):

$$E = \frac{C \times \Delta V^2}{2} \quad (3)$$

$$P = \frac{3600E}{\Delta t} \quad (4)$$

where E (W h kg^{-1}), C (F g^{-1}), ΔV (V), P (W kg^{-1}), and Δt (s) stand for energy density, specific capacitance, voltage window, power density, and discharge time, respectively.

1.3.2 OER performance

All electrocatalytic measurements were conducted on using three-electrode system in 1 M KOH aqueous solution. In this system, materials on NF (1 cm^2), Hg/HgO electrode and Pt plate were severed as working electrode, counter electrode and reference electrode, respectively. The polarization curves were conducted with the scanning rate of 5 mV s^{-1} of linear sweep voltammetry (LSV). All the potentials in this work were calibrated with respect to a reversible hydrogen electrode (RHE), and it could be deduced as follows: $E_{RHE} = E_{Hg/HgO} + 0.059pH + 0.098$. Tafel slopes could be got according the prominent equation ($\eta = a + blogj$) through the LSV curves. The electrical double-layer capacitance (C_{dl}) was acquired from CV curves between 0.36 to 0.44 V vs Hg/HgO. Electrochemical Active Surface Area (ECSA) was calculated by the equation: C_{dl}/C_s. The EIS tests were recorded under a frequency range of 0.01 to 10 000 Hz with an amplitude of 5 mV. Successive current step measurement at 10,

20, 50, 80, 100, 10 mA cm^{-2} proved its stability. The stability of as-prepared electrode for OER was measured by Chronopotentiometry at 10 mA cm^{-2}.

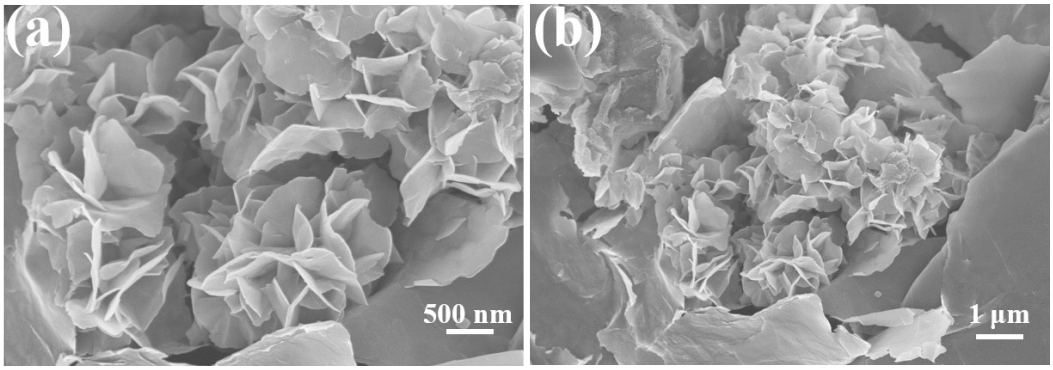

Figure S1 SEM images of $Co(OH)_2$.

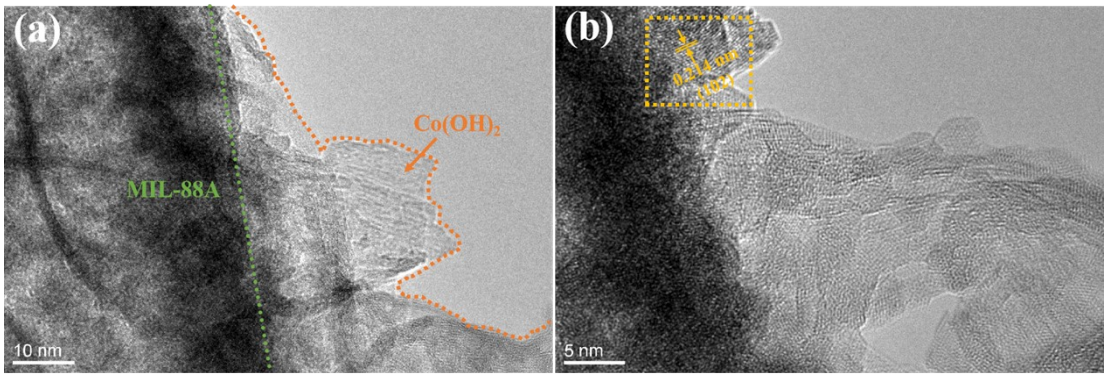

Figure S2 (a) TEM and (b) HRTEM of images of Fe-FA@$Co(OH)_2$.

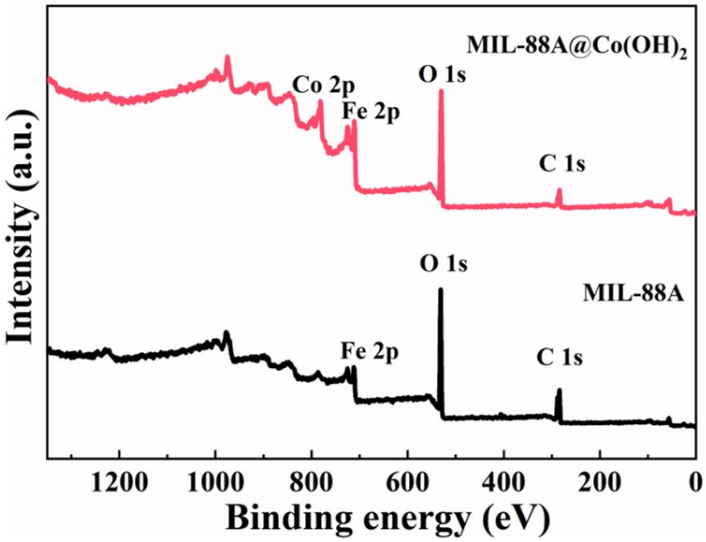

Figure S3 XPS spectra of Fe-FA and Fe-FA@$Co(OH)_2$.

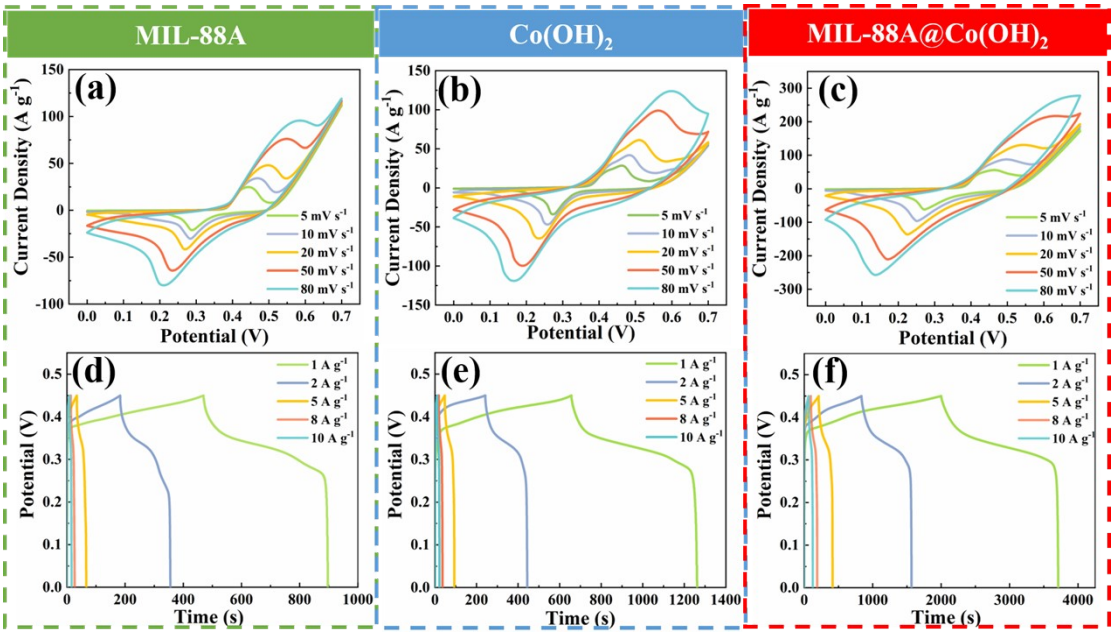

Figure S4 CV curves of (a) Fe-FA, (b) $Co(OH)_2$ and (c) Fe-FA@$Co(OH)_2$ at 5 to 80 mV s^{-1}; GCD curves of (d) Fe-FA, (e) $Co(OH)_2$ and (f) Fe-FA@$Co(OH)_2$ at 1, 2, 5, 8, 10 A g^{-1}.

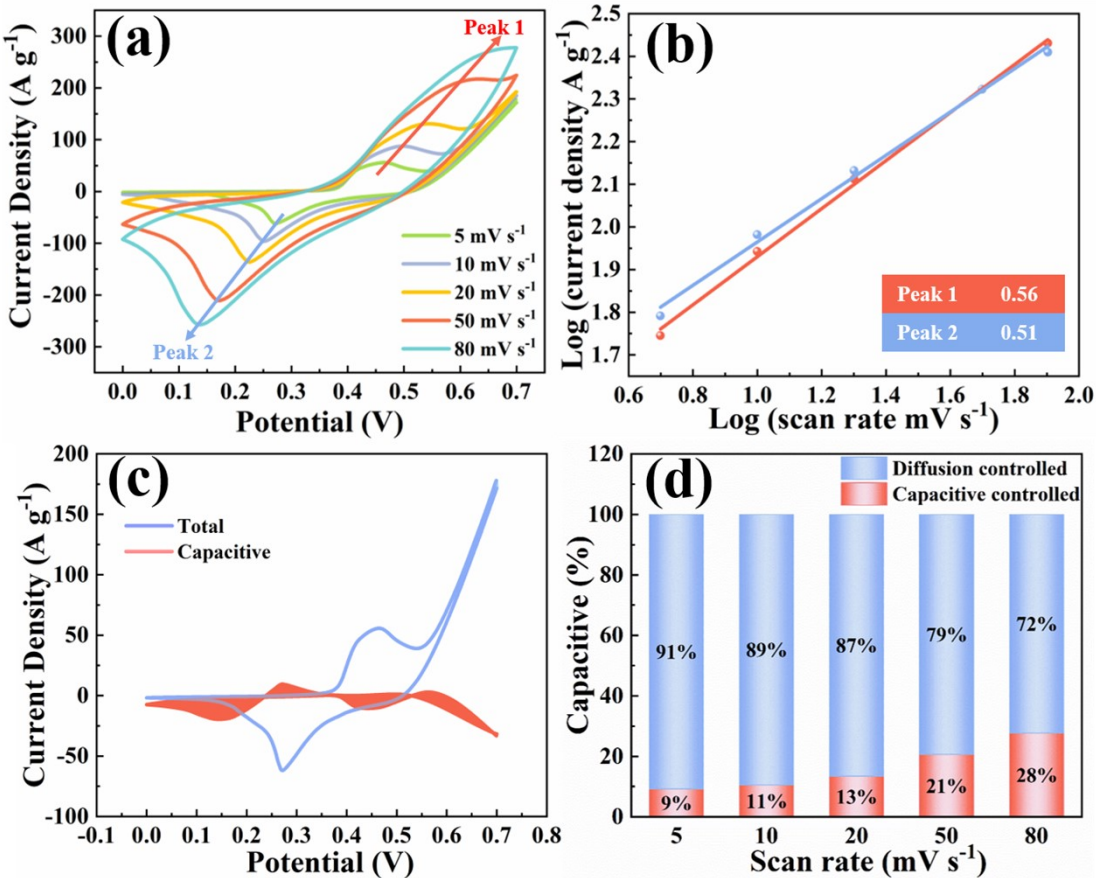

Figure S5 (a) CV curves of Fe-FA@$Co(OH)_2$ at 5 to 80 mV s^{-1}; (b) Relationship between logarithm peak current and logarithm scan rates; (c) Capacitive contribution and diffusion contribution at 5 mV s^{-1}; (d) Normalized contribution ratio of capacitive-controlled (blue) and diffusion-controlled (red) capacities at various scan rates.

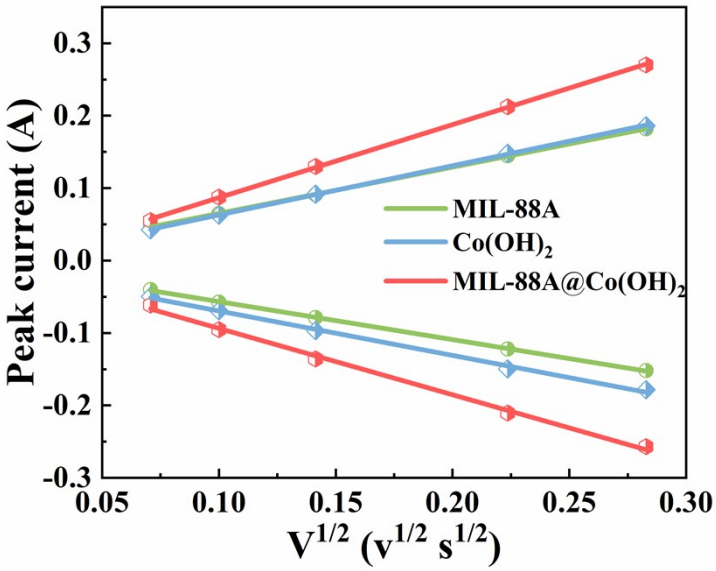

Figure S6 The relationship between the redox peak current and the square root of the scan rate

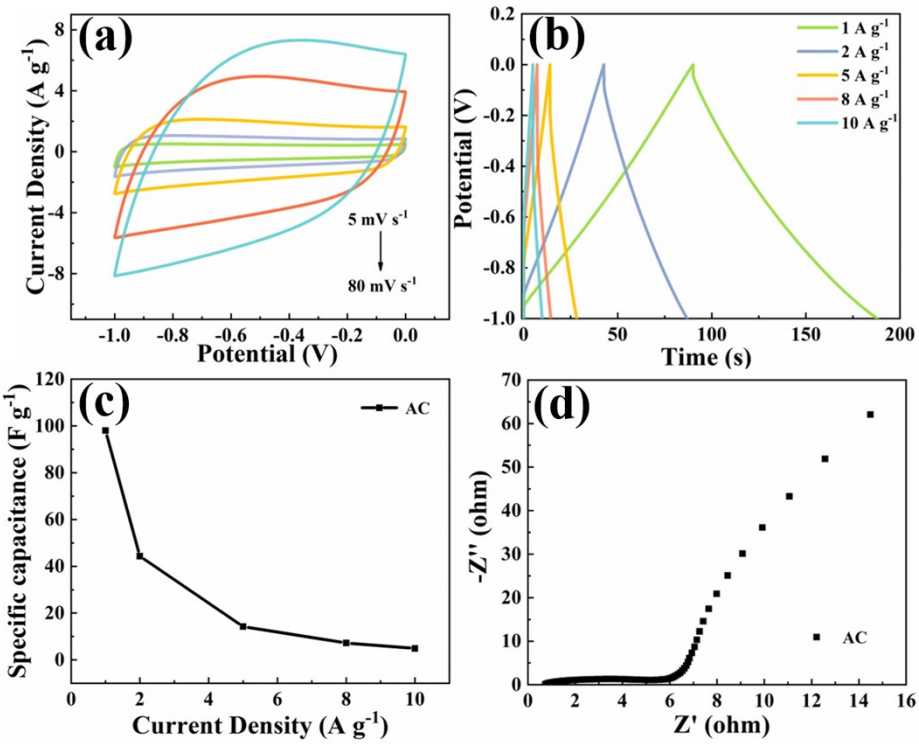

Figure S7 (a) CV curves of AC at different scan rate from 5 to 80 mV s^{-1}; (b) GCD curves of AC at 1, 2, 5, 8, 10 A g^{-1}; (c) Specific capacity of AC at different current densities; (d) EIS spectrum of AC.

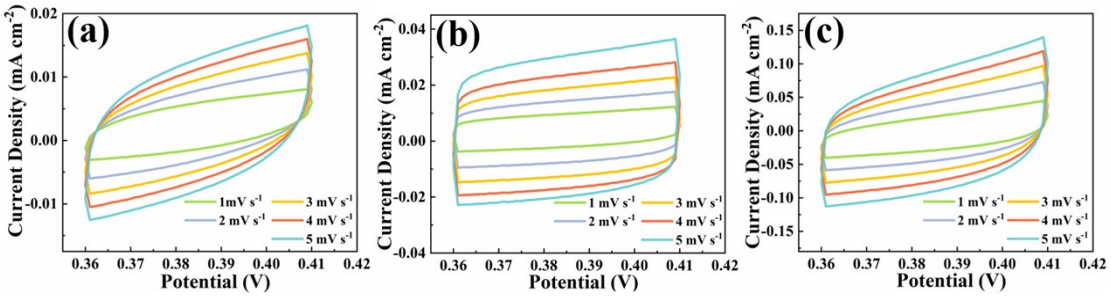

Figure S8. (a-c) CV curves at different scan rates of Fe-FA, $Co(OH)_2$ and Fe-FA@$Co(OH)_2$, respectively.

Table S1 Energy density and Power density of Fe-FA@$Co(OH)_2$/NF//AC/NF and other asymmetric supercapacitor.

Electrode	Energy density ($Wh\ kg^{-1}$)	Power density ($W\ kg^{-1}$)	Reference
Fe-FA@$Co(OH)_2$/NF//AC/NF	**77.84**	**800**	**This work**
$Ni_xCo_{1-x}(OH)_2$ // AC	**21.9**	**348.9**	**[2]**
$CoFe_2O_4$/rGO // AC	**12.14**	**643**	**[3]**
GAMOF(Fe^{3+})W // AC	**36**	**588**	**[4]**
CoFe hydroxides // AC	**28.3**	**512**	**[5]**
NiCo-MOF	**49.4**	**562.5**	**[6]**

Table S2 Comparison of the overpotential of different catalysts in OER process.

Electrode	Electrolyte	Overpotential (mV)	Reference
Fe-FA@Co(OH)$_2$	**1 M KOH**	**275**	**This work**
Cu-Co(OH)$_2$	**H_2-saturated 1 M KOH**	**310**	**[7]**
Co-MOF@Fe-FA	**1 M KOH**	**290**	**[8]**
NiCo-LDH	**0.1 M KOH**	**290**	**[9]**
Fe-CoOOH/G	**1 M KOH**	**330**	**[10]**
FeCo-MNS-1.0	**O_2-saturated 0.1 M KOH**	**298**	**[11]**
FeCo@C	**1 M KOH**	**302**	**[12]**
PI/CNT-Co(OH)$_2$	**O_2-saturated 0.1 M KOH**	**317**	**[13]**
aMoS$_x$/Co(OH)$_2$ NSs	**0.1 M KOH**	**350**	**[14]**
Fe$_2$Co-MIL-88B	**O_2-saturated 0.1 M KOH**	**348**	**[15]**
N-doped CoC$_x$/FeCo@C/rGO	**O_2-saturated 0.1 M KOH**	**390**	**[16]**

Reference

[1] X.F. Lu, L. Yu, X.W. Lou, Highly crystalline Ni-doped FeP/carbon hollow nanorods as all-pH efficient and durable hydrogen evolving electrocatalysts, Science Advances 5(2) (2019) eaav6009.

[2] S. He, Z. Li, J. Wang, P. Wen, J. Gao, L. Ma, Z. Yang, S. Yang, MOF-derived $Nix Co_1 - x(OH)_2$ composite microspheres for high-performance supercapacitors, RSC Adv. 6 (2016) 49478-49486.

[3] K.V. Sankar, R.K. Selvan, D. Meyrick, Electrochemical performances of $CoFe_2O_4$ nanoparticles and a rGO based asymmetric supercapacitor, RSC Adv. 5 (2015) 99959-99967.

[4] L. Liu, Y. Yan, Z. Cai, S. Lin, X. Hu, Growth-Oriented Fe-Based MOFs Synergized with Graphene Aerogels for High-Performance Supercapacitors, Adv. Mater. Interfaces 5 (2018) 1701548.

[5] X. Fang, S. Han, D. Liu, Y. Zhu, Two-dimensional CoFe hydroxides nanostructure as positive material for asymmetric supercapacitor, Chem. Phys. Lett. 746 (2020) 137282.

[6] Y. Wang, Y. Liu, H. Wang, W. Liu, Y. Li, J. Zhang, H. Hou, J. Yang, Ultrathin NiCo-MOF Nanosheets for High-Performance Supercapacitor Electrodes, ACS Appl. Energy Mater. 2 (2019) 2063-2071..

[7] L. Chen, H. Zhang, L. Chen, X. Wei, J. Shi, M. He, Facile synthesis of Cu doped cobalt hydroxide ($Cu–Co(OH)_2$) nano-sheets for efficient electrocatalytic oxygen evolution, J. Mater. Chem. A 5 (2017) 22568-22575.

[8] Y. Liu, C. Wang, S. Ju, M. Li, A. Yuan, G. Zhu, FeCo-based hybrid MOF derived active species for effective oxygen evolution, Prog. Nat. Sci. 30 (2020) 185-191.

[9] J. Jiang, A. Zhang, L. Li, L. Ai, Nickel–cobalt layered double hydroxide nanosheets as high-performance electrocatalyst for oxygen evolution reaction, J. Power Sources 278 (2015) 445-451.

[10] X. Han, C. Yu, S. Zhou, C. Zhao, H. Huang, J. Yang, Z. Liu, J. Zhao, J. Qiu, Ultrasensitive Iron-Triggered Nanosized Fe-CoOOH Integrated with Graphene for Highly Efficient Oxygen Evolution, Adv. Energy Mater. 7 (2017) 1602148.

[11] L. Zhuang, L. Ge, H. Liu, Z. Jiang, Y. Jia, Z. Li, D. Yang, R.K. Hocking, M. Li, L. Zhang, X. Wang, X. Yao, Z. Zhu, A Surfactant-Free and Scalable General Strategy for Synthesizing Ultrathin Two-Dimensional Metal-Organic Framework Nanosheets for the Oxygen Evolution Reaction, Angew. Chem., Int. Ed. Engl 58(38) (2019) 13565-13572.

[12] Q. Wu, T. Li, W. Wang, Y. Xiao, High-throughput chainmail catalyst FeCo@C nanoparticle for oxygen evolution reaction, Int. J. Hydrog. Energy 45 (2020) 26574-26582.

[13] Y. Jiang, X. Li, T. Wang, C. Wang, Enhanced electrocatalytic oxygen evolution of alpha-$Co(OH)_2$ nanosheets on carbon nanotube/polyimide films, Nanoscale 8 (2016) 9667-9675.

[14] F. Sun, C. Li, B. Li, Y. Lin, Amorphous MoSx developed on $Co(OH)_2$ nanosheets generating efficient oxygen evolution catalysts, J. Mater. Chem. A 5 (2017) 23103-23114.

[15] C. Wu, X. Zhang, H. Li, Z. Xia, S. Yu, S. Wang, G. Sun, Iron-based binary metal-organic framework nanorods as an efficient catalyst for the oxygen evolution reaction, Chinese J. Catal. 42 (2021) 637-647.

[16] H. Fang, T. Huang, Y. Sun, B. Kang, D. Liang, S. Yao, J. Yu, M.M. Dinesh, S. Wu, J.Y. Lee, S. Mao, Metal-organic framework-derived core-shell-structured nitrogen-doped CoC_x/FeCo@C hybrid supported by reduced graphene oxide sheets as high performance bifunctional electrocatalysts for ORR and OER, J. Catal. 371 (2019) 185-195.